Data set generation at novel test-rig for validation of numerical models for modeling granular flows

Widuch Agata, Myöhänen Kari, Nikku Markku, Nowak Marcin, Klimanek Adam, Adamczyk Wojciech

DOI: 10.1016/j.ijmultiphaseflow.2021.103696

Data set generation at novel test-rig for validation of numerical models for modeling granular flows

Agata Widuch[a], Kari Myöhänen[b], Markku Nikku[b], Marcin Nowak[a], Adam Klimanek[a], Wojciech Adamczyk[a,*]

[a]*Silesian University of Technology, Faculty of Energy and Environmental Engineering, Department of Thermal Engineering, Konarskiego 22, 44-100 Gliwice, Poland*
[b]*LUT School of Energy Systems, Lappeenranta University of Technology, Post Office Box 20, FI-53851 Lappeenranta, Finland*

Abstract

Significant effort has been exerted on developing fast and reliable numerical models for modeling particulate flow; this is challenging owing to the complexity of such flows. To achieve this, reliable and high-quality experimental data are required for model development and validation. This study presents the design of a novel test-rig that allows the visualization and measurement of particle flow patterns during the collision of two particle streams. Valuable data sets are provided for the validation of numerical models dedicated to granular flows. The experimental work was conducted for three particle distributions and different configurations of the test rig setup. Additionally, a standard discrete element method for modeling particle transport was applied to the test-rig configuration and the effects of the material spring constant on the predicated flow patterns are investigated. An additional purpose of these simulations was also to collect necessary data for further collision model validation, developed based on a reduced-order technique.

Keywords: particle collision, DEM, experimental work, particle tracking, CFD

*Corresponding author: Wojciech Adamczyk wojciech.adamczyk@polsl.pl

DOI: 10.1016/j.ijmultiphaseflow.2021.103696

Nomenclature

u	velocity, m/s	$\mathbf{u}$	velocity vector, m/s
K	spring constant, N/m	d_p	particle diameter, m
F	force, N	K	interphase drag coefficient, -
F_D	drag coefficient, 1/s	K	interphase drag coefficient, -
M	atomic mass, kg/kmol	T	temeprature, K
m	mass flow rate, kg/s	R	universal gas constant, J/(kmol·K)
V	volume, m^3	p	pressure, Pa
$\mathbf{e}$	unit vector, -	A	area, m^2
ρ	density, kg/m^3	τ	time, s
δ	overlap distance, m	α	friction coefficient, -
γ	damping coefficient, -	η	restitution coefficient, -
ε	volume fraction, -	σ	stress tensor, -
Abbreviations			
CFB	Circulating Fluidized Bed	KTGF	Kinetic Theory of Granular Flow
CFD	Computational Fluid Dynamics	PSD	Particle Size Distribution
CPFD	Computational Particle Fluid Dynamics	HEL	Hybrid Eulerian-Lagrange
DEM	Discrete Element Method	EE	Eulerian-Eulerian
FM	Flow Meters	TA	Time Average
BH	BronkHorst		
Subscripts			
init	Initial value	f	fluid
p	pParticle	s	Solid - dispersed phase
coll	Particle collision	c	Numerical cell

1. Introduction

Particulate flow is used in multiple practical applications. It can be found in the research branch, petroleum, chemical, health care industry (manufacturing of drugs), food processing industry, and energy sector, such as heat production in the circulating fluidized bed (CFB). In addition to the intensive development and improvement of production technologies, several problems remain. An example is fluidization technology characterized by the highly loaded particulate flow. Although CFB technology is mature and the CFB boilers have been developed to utility-scale, they still suffer from some deficiencies, such as erosion, non-uniform or unstable flow conditions, and bed maintenance problems, which affect the boiler availability and overall performance [1, 2].

Nowadays, enormous efforts have been put into the development of engineering tools and models, which can be used to improve processes to solve problems with their imperfections, reduce emissions of harmful species, and increase efficiency. Well-optimized processes allow the reduction of COPEX (capital expenditures) and OPEX (operating expenditures), which is highly demanded by investors. To achieve this, reliable simulation tools are required for new designs or to upgrade existing systems/processes. Computational fluid dynamics (CFD) has been successfully utilized for this purpose [3]. However, the simulation of multiphase processes has proven challenging owing to the wide temporal and spatial scales found in the suspension flow, the strong coupling of gaseous and solid phases, and the complex interactions between particles [4, 5].

It is apparent that numerical modeling of particulate transport within large-scale installations, as well as in laboratory devices, is complex, expensive, and challenging [6]. All of the available computational techniques, i.e., two-fluid Euler-Euler approach [7], hybrid Eulerian-Lagrangian (EL) [8, 9, 10], or discrete element method (DEM) [11, 12], suffer from deficiencies, mainly in the prediction of particle-particle collisions. The first two of these models to model the gas-solid interactions require additional constitutive relations and closure laws. The kinetic theory of granular flow (KTGF) [13, 14] — developed based on the theory of dense gases [15] — has been commonly applied to deriving the constitutive relations for the interactions between particles (e.g., collisions) as

well as between granular and fluid phases. Within the collision model, the particles are assumed to be perfectly smooth spheres, and particle–particle collisions can be described by a single parameter. Only the normal impact and rebound velocities of two colliding particles are related, using the coefficient of restitution, while the changes to particle velocity in the tangential direction are neglected by the model [16]. A straightforward approach for modeling particle interactions is to apply the discrete element method (DEM) [11, 17, 18, 19], which predicts collisions between particles at low levels. Besides the advantages of the DEM approach, numerous issues need to be resolved. The biggest concern is calculation time since this model requires an accurate definition of the time step to solve the particle motion equation and define the collision model parameters, depending on the selected mathematical model. To obtain accurate results in terms of collision prediction, extremely small time steps are required (10^{-6}) to solve the particle motion equation. Over the years particle collision models for a range of particle interactions and carrier fluid flow conditions have been developed. Interesting overview of development process can be found in [20]. In that work various limitation of existing approach also have been discussed.

Clearly, an approach that allows for the possibility of reducing calculation time while maintaining the required accuracy is desirable to accurately model the particulate flows [21]. To deal with these complexities, a new approach for predicting particle collisions is extremely worthwhile to reduce the numerical simulation cost. The presented work is the initial step towards developing a collision model that will allow simulation of the particle interactions with the accuracy of the DEM approach, with the simulation time of the hybrid Euler-Lagrange approach ($\Delta\tau$ at the level of 10^{-3}). This will be achieved by replacing the standard KTGF model [13] used for prediction of the particle interaction in the hybrid Euler-Lagrange approach with the surrogate collision model (reduced order model (ROM)), developed based on the data collected using an accurate and validated DEM approach. Farther developed ROM will be built applying Deep Machine Learning [22] technique, where it will by validated against experimental data discussed in this paper. As the numerical results can be affected by the uncertainty in input data to CFD simulations, i.e. mass flow rates of the air delivered to the rig that affect velocity in the core section of the rig, material properties like as Young module, spring constant, Poisson constant or the collision space (volume where the collision is detected) also the validation and uncertainty quantification (VUQ) [23] will be used.

To test the behavior of the developed numerical model, the calculated data need to be juxtaposed with experimental data. Available literature data are mostly focused on testing particle clustering phenomena to accurately predict flows within the riser [24, 25, 26, 27] and improvements on drag models responsible for modeling particle distribution over lab-scale installations [28]. In terms of application of DEM approach for modeling particulate flows used models are mostly validated globally using dedicated case. An example can be found in [29] where DEM approach was validated modeling the mill where the breakage process of particle was investigated.Interesting study can be also found in [30] where an extended three-dimensional model to describe the process of wall collisions of arbitrary shaped non-spherical particles was investigated. Obtained numerical results have been compared against experimental data applying results discussed in [31]. Other example where DEM approach is tested against experimental results can be found in [32], where a screw feeder system was simulated.

The purpose of this work was to manufacture a novel test rig to visualize and investigate particle flow patterns during collisions, where two streams of solid particles made form polyethylene material at a given angle collide in the center of the test-rig. The novel test-rig design is based on the description of the numerical investigation by [33]. The configuration of the test rig allows the tracking of particles during the collision process applying high speed camera. Test-rig configuration gives possibility to track the particle velocity profiles in different cross-section, arbitrary selected downstream from particle injection port. One of the biggest concern while particulate system are investigated are obstacles with efficient procedure that can be used to track changes of particle velocity. To automatize the tracking procedure, an *in-house* application, developed in National Instrument LabVIEW (National Instruments Corp., USA) [34]. has been used for tracking particle motion. Part of this work is focused on providing explanation about the test-rig design together with a wide range of experimental data description that can be used for testing the accuracy and feasibility of the numerical models dedicated to modeling particulate flows. Test-rig and equipment can be also used to provide micro-scale data (collision between subsequent particles) in the case of low level mathematical model developments. Within the second part of this paper the attention is directed on application of the numerical model, here the DEM approach to simulate particulate flow of the test-rig configuration. The set of numerical results were compared against experimental data. The set of numerical simulation presented in this article was made applying DEM approach available in Ansys® Fluent

[35]. It is worth to mention here that even application of commercial CFD code it is not trivial task to carried out the simulation. In order to reach stable conditions operational parameters, setup of the mathematical model need to be carefully investigated and selected. Here the soft-sphere collision model, where particle-particle as well as particle-wall interaction were controlled applying spring constant [36], where impact of this parameter on predicted particle velocity profiles was studied. We need to collect the necessary knowledge of how the DEM approach works and how it is sensitive to changing model parameters — i.e., material properties, such as the spring constant — to use it as the core model for generating data to construct, a surrogate model for predicting particle interactions. Farther developed surrogate model will be implemented into the Ansys® Fluent code in order to efficiently and accurately simulate particle interactions.

2. Experimental facility

Experimental work was conducted with a novel laboratory-scale test rig presented in Fig. 1. The test rig was designed and built based on the numerical model discussed in O'Rourke et al. 2010 [33], used for testing different model parameters on the particle collision process. To ensure the stable operation required for the test rig, modifications were made to the original design. For particle tracking, the measurement section of the rig was constructed from transparent polycarbonate. The airflow was controlled by three precise Bronkhorst HIGH-TECH B.V. [37] mass flow controllers. Two smaller units (BH1 and BH2), operating in the range 1.2—60.0 ln/min (F-201AV-50K-VBD-00-V), were used to control the flow rate in the injection tubes (Fig. 2). The largest unit (BH3) was used for the core flow, with a range of 7.2—360.0 ln/min (F-203AV-M50-VBD-00-V) (Fig. 2).

To capture the particle trajectories, a high-speed camera VEO 710L [38] was equipped with a NIKKOR 200 mm F/4.0 MACRO lens. This configuration allowed the tracking of particles at a resolution of 832 x 600 pixels and a rate of 14,000 frames per second. To ensure sufficient illumination for the camera, a back-light (LED Phlox HSC Phantom 10 x 10 cm) was used with a luminance of ≥130.000 cd/m^2, uniformity of ≥ 95%, and light temperature of 5,700 K.

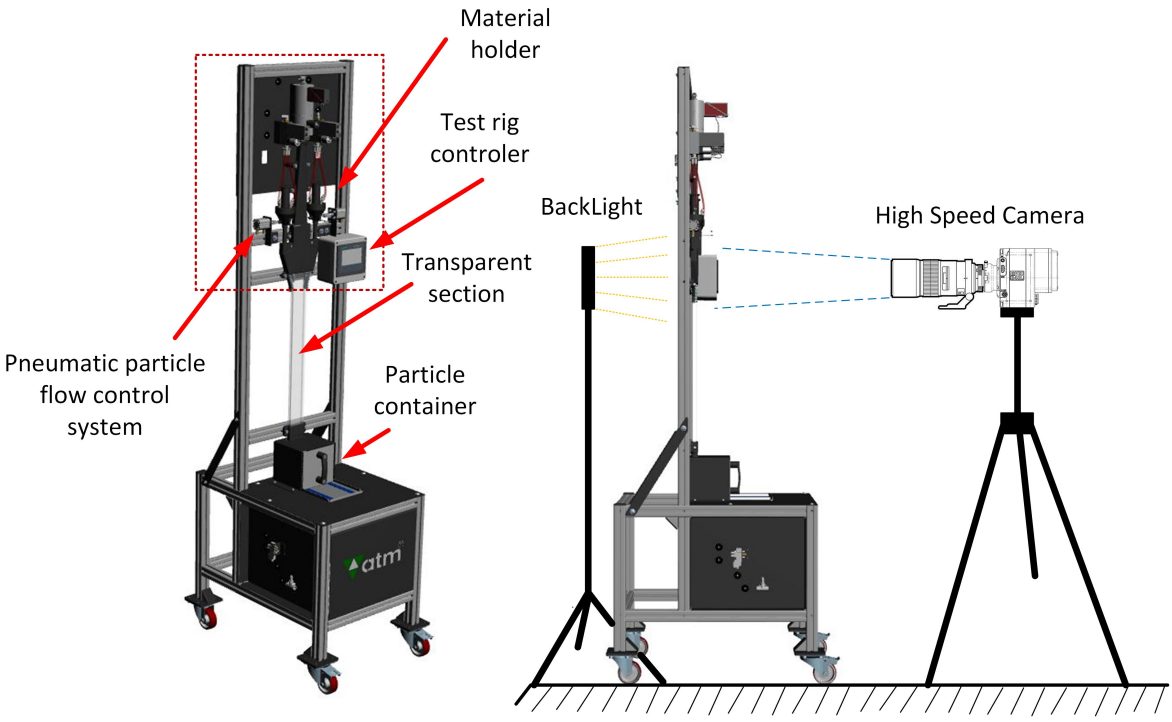

Figure 1: The test rig configuration with the main elements marked

The dimensions of the rig are presented in Fig. 2. The cross-section of the core channel is 50 x 4 mm, allowing for a superficial gas velocity of up to ∼30 m/s. The cross-section of the injection tubes is 8 x 4 mm, allowing for superficial gas velocities of up to ∼30 m/s. To ensure a uniform velocity profile within the measurement section, a long divergence nozzle was used to convert the flow channel from the circular inlet to a rectangular cross-section. The nozzle and injection tube design was supported by CFD analysis with ANSYS Fluent to ensure even flow profiles and stability, as well as mixing rates.

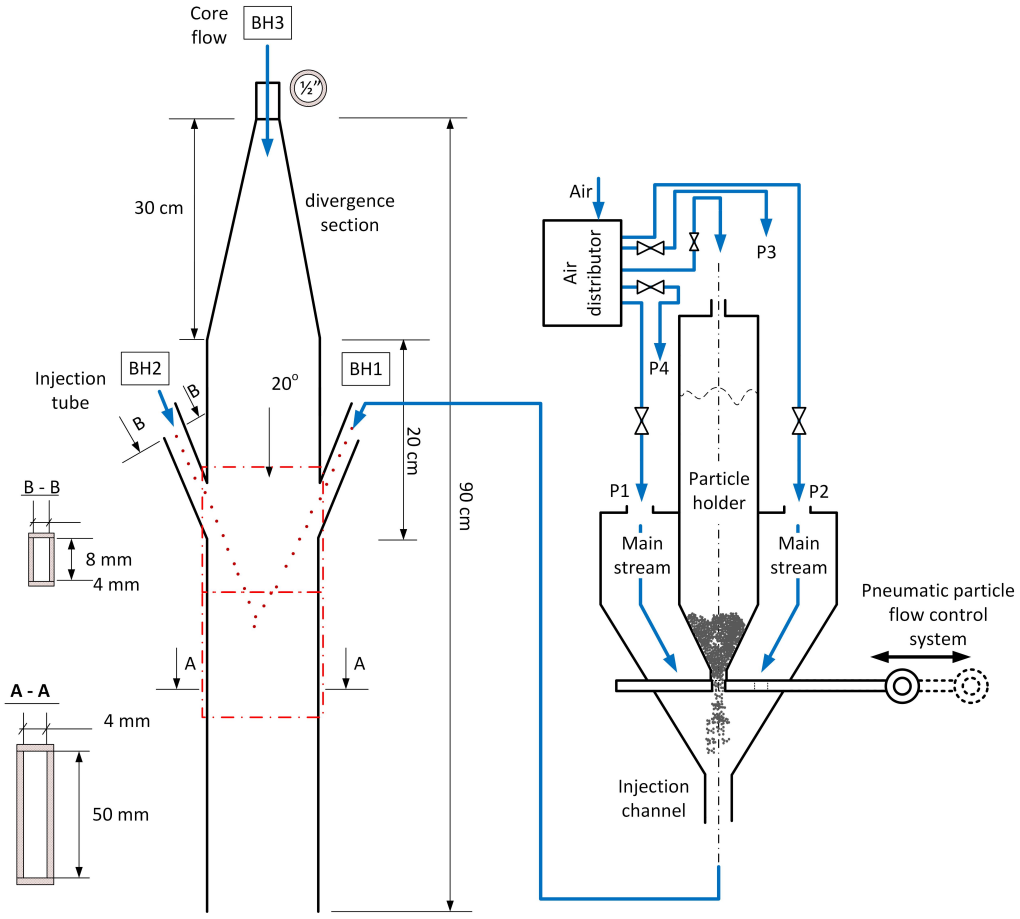

Figure 2: Dimensions of the test rig (on the left) and the particle feeder (on the right)

The particle feeder is illustrated in Fig. 2. The construction was 3D-printed to ensure a high degree of accuracy for the carefully designed gas flow paths. The particle holders/feeders are placed on both sides of the core channel. Each particle holder stores 15 g of material, which is sufficient for up to 3 s of testing. The air is delivered with five different lines to control the gas distribution. 10% of the total air is delivered to the particle holder to maintain a small overpressure in the particle holder and enable the particles to be fed into the injection channel. The other four lines (P1, P2, P3, and P4) enter the main stream to disperse the particles and control the momentum of the particles.

The test rig was controlled using Siemens SIMATIC S7−1200. The following measurement procedure was followed for each measurement:

- the core flow was started and the flow was allowed to stabilize for 2−5 s,
- the injection airflows were started and allowed to stabilize for 5−10 s,
- the injection bar blocking the particle holder was removed and the high speed camera recording was started as particles started to flow through the injection channel.

The selected test material was gray polyethylene microsphere particles [39]. This type of material is characterized by an almost perfectly spherical shape. Tab. 1 presents the particle size data provided by the manufacturer. Six different test cases with varying particle sizes and flow rates were performed, as indicated in Tab. 2. In each case, the tests were repeated three times (test points A, B, and C).

	300—355	425—500	500—600
Largest diameter, μm	354	520	654
Smallest diameter, μm	300	429	504
Mean diameter, μm 2	315	475	562
Median diameter, μm	314	473	559
Standard deviation, μm	8.2	22	32

Table 1: Particle size information of the polyethylene microspheres

	Particle size, μm	Flow rate, ln/min (Injection/Core)
Case 1 (A, B, C)	300—355	38.4/100.0
Case 2 (A, B, C)	300—355	45.0/100.0
Case 3 (A, B, C)	300—355	55.0/100.0
Case 4 (A, B, C)	300—355	38.4/240.0
Case 5 (A, B, C)	425—500	38.4/240.0
Case 6 (A, B, C)	500—600	38.4/240.0

Table 2: Investigated configuration of the input parameters of the rig

2.1. Image analysis

Particle tracking in dense flow is an extremely demanding task. To track and determine the particle velocity profiles, a dedicated application was written in the National Instruments LabVIEW software. The application allows for a convenient and very efficient method of comparing simulated and measured data, based on the particle velocity profiles calculated within three selected frames (locations), as illustrated in Fig. 5. This is an important step towards applying uncertainty analysis, where a dozen simulations need to be conducted to determine the impact of uncertainty in experimental data on predicted numerical results. Nevertheless, this is not a subject of current work but such analysis will be conducted in the future. Without such a procedure, manual analysis of experimental and numerical results would be extremely time-consuming.

To determination of particle velocity a procedure depicted in Fig. 4 is used. Particle tracking procedure initially converts a grayscale image into a binary image with a defined threshold, which can slightly differ for simulated and experimental data. This threshold is defined once at the beginning of the conversion procedure and remains constant for all analyzed cases. In order to check the influence of threshold range used for experimental data two configuration of its value were investigated. Firstly, the minimum and maximal values where taken when particles are seen without iterating with the background. Secondly, value of threshold was taken in the middle of this range. For configuration of the rig, i.e. used camera and backlight system the threshold range effect was marginal. Nevertheless, after changing configuration of the rig this need to be always verified. Here the backlight intensity and setups of the simulations remain unchanged for all investigated cases. Using the binary image, the position of each detected particle can be found. To reduce the cost of tracking individual particles, only the particles located within the predefined frames are analyzed. An example of a detected particle in a single image at time 0.0621 s can be seen in Fig. 3, highlighted in green. For known location of the particles in given time step, next part of the tracking procedure can be activated as it is shown in Fig. 4. Firstly, the maximal distance that particle can travel within a considered frame is defined both horizontally (x_{max}) and vertically (y_{max}). Both dimensions are specified based on the observation of particle movement at the beginning manually checking recorded frames. Next, tracking box, where it left vertical edge is located at the center of every detected particle in a considered time step, illustrated as blue box in Fig. 4. Within next time step, within investigated region particle

is detected. Here question can be formulated. Mainly, what happen when several particles will be detected in defined frame in fallowing time step? Such situation can be true when for instance some particles will fly into the box outside considered region. Here, the problem is solved by definition of minimal and maximal distance that particle can travel. This admissible traveling distance was defined based on observation of the experimental data. Particle which will travel to faraway or will be located to close to originally detected particle are rejected. The accuracy of the procedure can be questionable, because several parameters need to be defined. Even that inconvenience, in case of necessity of tracking dozen of experimental results without having such procedure, results analysis will be awkward. In order to check procedure accuracy, velocities were also calculated manually and compared with those obtained automatically, this has been done only for selected cases. Having the location of the particle in the next time step the particle velocity in two direction can be determined and next the velocity magnitude can be determined. As it was mentioned this procedure does not eliminate situations where two or more particles will be detected per given time step within an investigated region. In order to prevent such a situation, the number of tracked particles in each frame is counted and in case of a more than 10% increase in the number of located particle between frames, the investigated region size is adjusted. Moreover, if the distance the particle traveled during a time step is shorter than that seen during manual analysis, those particles are eliminated from calculation as it was mentioned.

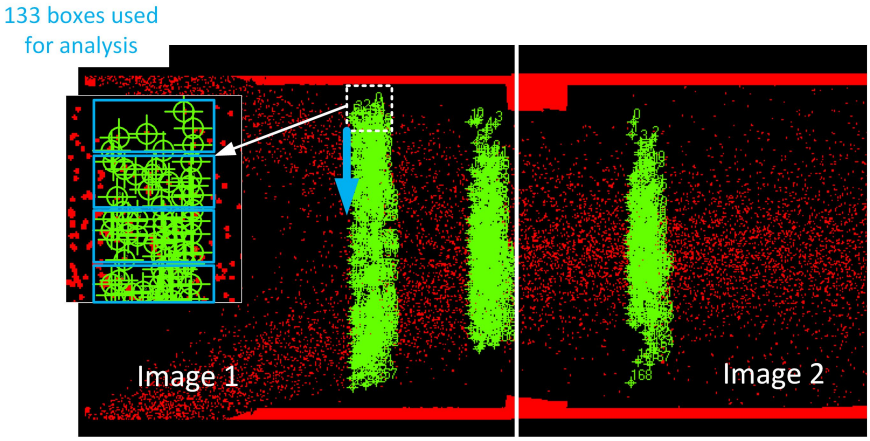

Figure 3: Particles detected from the binary image highlighted in green with the analysis boxes used for particle tracking

Owing to the limited field of view (FOV) of the camera, the observation region was divided into two frames, which were later built together, as shown in Fig. 5. The image overlapping procedure, which is crucial for data comparison, was also developed within the framework of the LabVIEW application, using the Vision toolbox. Frame positions used in the data analysis were selected based on observations of the particle flow patterns within the domain during the experimental work. In the first frame, two separated particle streams can be distinguished. In the second frame, intensive particle interactions between the two streams are noticeable while the third frame presents a uniform flow pattern.

To calculate the time-averaged particle velocity profiles within the considered frame, it is vertically divided into a finite number of boxes (see Fig. 3); in this case, 133 boxes were used. The tracking procedure calculates the average particle velocities separately for each box for a subsequent time step, which is then stored in memory. It is clear that the average particle velocity calculated within the initial time steps does not represent the particle velocities of the developed flow as it takes time before the flow profiles stabilizes. Even after stabilization, the particle velocities fluctuate within subsequent time steps. To mitigate this effect, the time-average (TA) procedure is used at the end of the tracking procedure to calculate the time average particle velocities in a given box. The

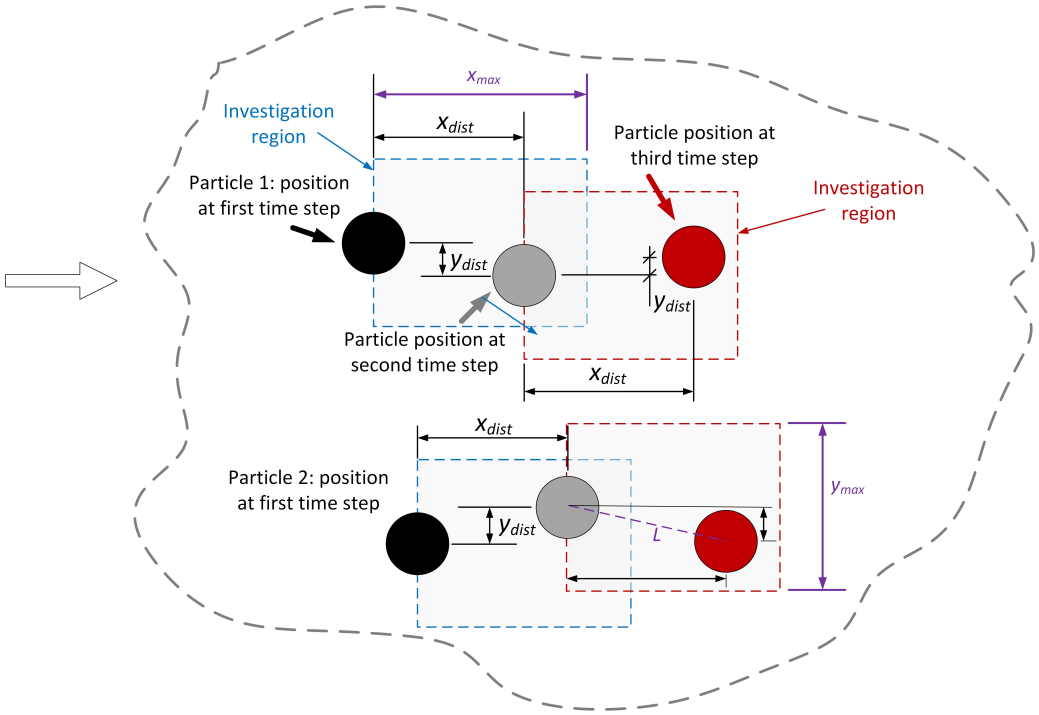

Figure 4: Particle tracking procedure used for calculating the particle velocity

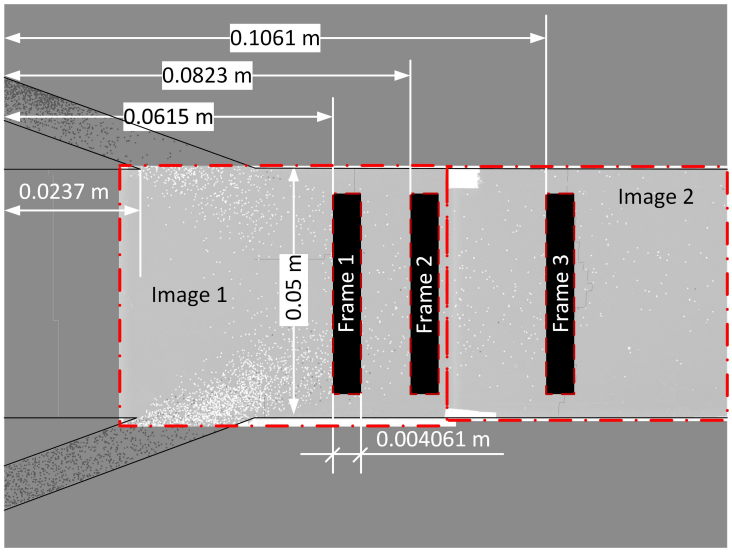

Figure 5: Locations of the frames used to calculate particles velocities

time average particle velocity in a given box was calculated as

$$\begin{aligned} \phi_{time,i+1} &= \phi_{\text{time},i} + \phi_i \cdot \Delta\tau_i \\ u_{TA} &= \frac{\phi_{time,i} - \phi_{time,i-n}}{\tau_i - \tau_{i-n}} \end{aligned} \tag{1}$$

where ϕ denotes the averaging variable — in this case, it is velocity — and u_{TA} denotes the time-averaged velocity.

These equations allow the time-averaging of any variable during simulation or post-processing. To verify whether the flow has stabilized, the average particle velocity fluctuations were monitored over the given time steps.

2.2. Uncertainty analysis of the experimental data

An important step in experimental procedures is calculating the uncertainty of the experimental data. This is very important in the case of numerical model validation to determine the consistency range between the results. Without this information, it is extremely difficult to fit the numerical model into the exact experimental data. The error bars for the subsequent experimental data set help to verify the applicability of the numerical results.

First, the uncertainty stemming from using the digital camera has been investigated. For the used device, the factors that affect uncertainty are pixel size ($u_x = 0.02$ mm) and image acquisition rate, calculated as

$$u_\tau = \frac{\Delta u_{TA}}{\Delta \tau_{TA}} \cdot \Delta\tau \tag{2}$$

where Δu_{TA} is the maximal velocity change observed during the period used for time-averaging (TA) calculated for $\Delta\tau_{TA}$ equal to 0.0321 s, which corresponds to 450 frames, and $\Delta\tau = 7.14286E{-}05$ s is the time step between subsequent frames. The uncertainties due to the measured velocity depend upon the accuracy of the mass flow controllers (FM) u_{FM}, defined as $\sigma_{FM} \pm 0.5\%$. Hence, the uncertainty u_{FM} can be calculated as

$$\begin{aligned} u_{u,min} &= \frac{m_{min}}{A_{tube} \cdot \rho_{air}} \quad \text{where} \quad m_{min} = \frac{V_{n,min} p M_{air}}{RT} \\ u_{u,max} &= \frac{m_{max}}{A_{tube} \cdot \rho_{air}} \quad \text{where} \quad m_{max} = \frac{V_{n,max} p M_{air}}{RT} \\ u_{FM} &= u_{u,max} - u_{u,min} \end{aligned} \tag{3}$$

where p is the pressure equal to 101.325 kPa; T is the temperature of gases within the rig ~298 K, M_{air} is the atomic weight of air 28.84 kg/kmol, R is the universal gas constant (8314 J/(kmol·K)), ρ_{air} is the air density under real conditions, and $V_{n,min}$ and $V_{n,max}$ are the volumetric flow rates under normal conditions ($p_n = 101325$ Pa, $T_n = 273.15$ K). The methodology was applied to the mass flow controllers attached to the tube injectors $u_{FM,tube}$ and core section $u_{FM,core}$. The total uncertainty of the measured gas velocity u_u is the result of the law of error propagation, which is defined as [40]

$$\begin{aligned} u_u^2 = &\left(\frac{\partial u}{\partial x}\right)^2 u_x^2 + \left(\frac{\partial u}{\partial \tau}\right)^2 u_\tau^2 + \left(\frac{\partial u}{\partial l}\right)^2 u_x^2 + \\ &2\frac{\partial u}{\partial x}\frac{\partial u}{\partial \tau}\mathrm{cov}(x,\tau) + 2\frac{\partial u}{\partial x}\frac{\partial u}{\partial l}\mathrm{cov}(x,l) + \\ &2\frac{\partial u}{\partial l}\frac{\partial u}{\partial \tau}\mathrm{cov}(l,\tau) + u_{FM,tube}^2 + u_{FM,core}^2 \end{aligned} \tag{4}$$

where subscript x, τ, and l refer to pixel location, time, and length (in the x direction: x_{dist}) of the box used for the velocity calculation. The covariance cov accounts for the correlation between time and space. In the considered case, these quantities are not correlated and so the covariance vanishes and the equation simplifies to

$$u_u = \sqrt{\left(\frac{\partial u}{\partial x}\right)^2 u_x^2 + \left(\frac{\partial u}{\partial \tau}\right)^2 u_\tau^2 + \left(\frac{\partial u}{\partial l}\right)^2 u_x^2} + u_{FM,tube} + u_{FM,core} \tag{5}$$

The uncertainties collected in Table 3 correspond to the maximum values of the partial derivatives in the range of space and time intervals used in the experiments. Thus, the uncertainties are conservative.

3. Experiment

This section discusses the experiments conducted for a wide range of operating parameters. To investigate the influence of different conditions in the test rig, the particle velocity profiles were measured within three locations

Analyzed case	$\frac{\partial u}{\partial x}$, $\frac{1}{s}$	$\frac{\partial u}{\partial \tau}$, $\frac{m}{s^2}$	$\frac{\partial u}{\partial l}$, $\frac{1}{s}$	u_τ, s	$u_{FM,tube}$, $\frac{m}{s}$	$u_{FM,core}$, $\frac{m}{s}$	u_u, $\frac{m}{s}$
Case 1 (A, B, C)	3.342	9.333	6962.5	6.67E-04	0.199	0.235	0.638
Case 2 (A, B, C)	4.456	12.444	6075.0	8.89E-04	0.234	0.235	0.669
Case 3 (A, B, C)	4.223	11.822	5959.9	8.44E-04	0.286	0.235	0.716
Case 4 (A, B, C)	4.679	13.067	6598.8	9.33E-04	0.199	0.434	0.808
Case 5 (A, B, C)	3.565	9.955	4907.2	7.11E-04	0.199	0.434	0.756
Case 6 (A, B, C)	2.228	6.223	3503.5	4.44E-04	0.199	0.434	0.716

Table 3: Calculated uncertainties for investigated materials based on the law of error propagation

of the analyzed field of view. An important factor during the experimental work is to ensure the repeatability of the collected data. For that purpose, every test with a given set of conditions was repeated three times. The collected data were then used for evaluating particle velocity profiles via an in-house application. For the collected profiles, the average particle velocities and standard deviations were computed.

The first set of experiments was conducted with particles classified in PSD 300—355 μm, which is a typical particle size range for CFB units [41]. The calculated time-averaged particle velocity profiles and standard deviations for four cases — 1st, 2nd, 3th, and 4th — are illustrated in Figs. 6 and 7, respectively. It can be seen that increasing the gas velocity affects the velocity profile, mainly at the first and third locations, corresponding to Frames 1 and 3. For the first three cases, the flow rate of the gas at the injection tubes increased, which resulted in displacement of the downstream collision region, which also can be clearly seen in Fig. 8. In the core, the particles accelerate owing to the higher velocity of the gas. By increasing the core flow rate in the fourth case, the particles reach higher velocities at the third location, unlike in other cases. Within the second location, the flow stabilizes for the first three investigated cases while, in the fourth case, the particle velocities stabilized at the third location. The experiments were repeatable, as confirmed by the calculated standard deviations presented in Figs. 6 and 7, respectively. For an overwhelming majority of the analyzed boxes for three frames, the calculated standard deviation based on the calculated particle velocities for three repeated tests — A, B, and C — were smaller than 0.2 m/s.

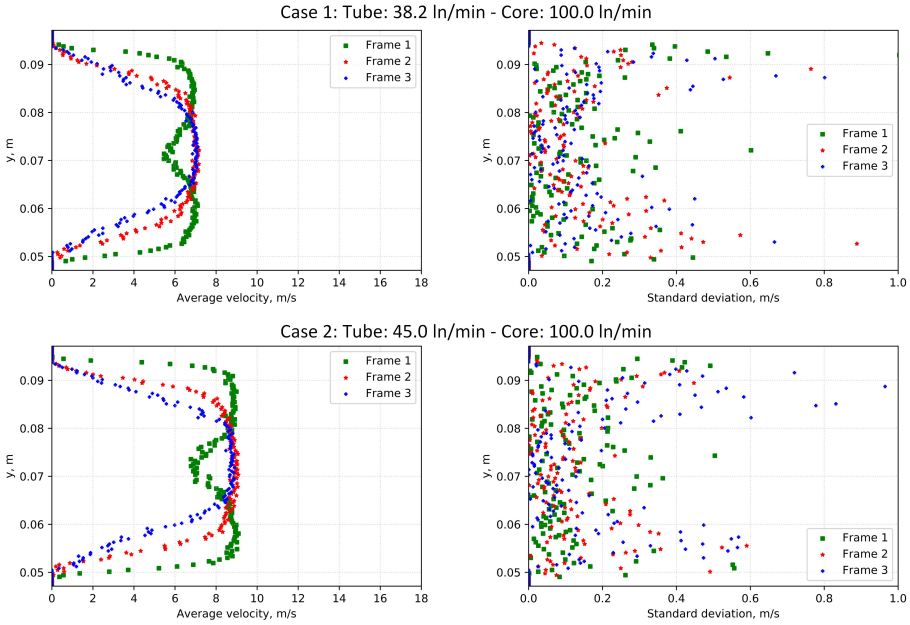

Figure 6: Calculated average particle velocity profiles (left column) and standard deviations (right column) for PSD 300—355 μm and 1st and 2nd cases based on measured velocity profiles during repeatability tests

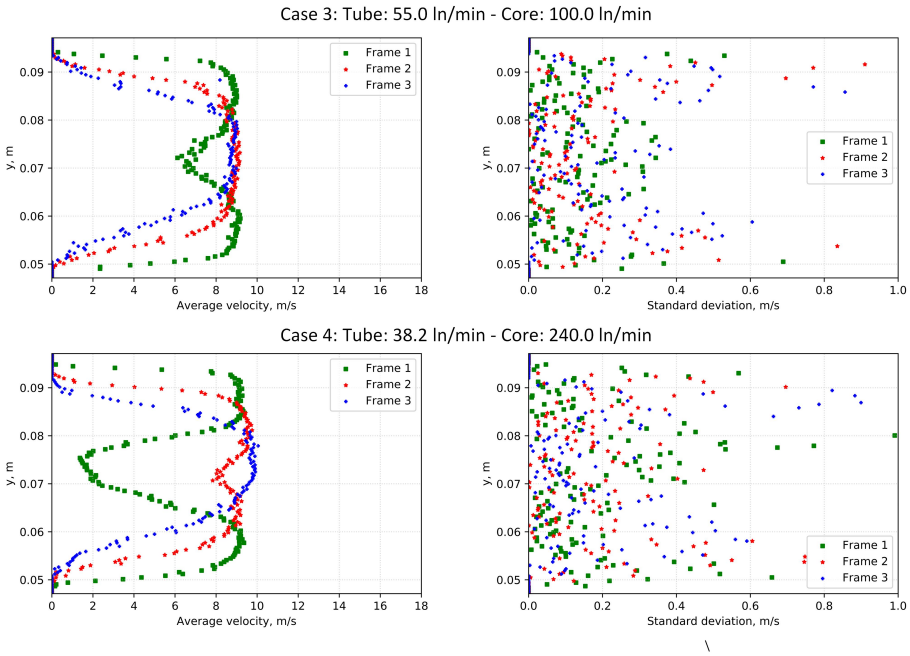

Figure 7: Calculated average particle velocity profiles (left column) and standard deviations (right column) for PSD 300–355 μm and 3th and 4th cases based on measured velocity profiles during repeatability tests

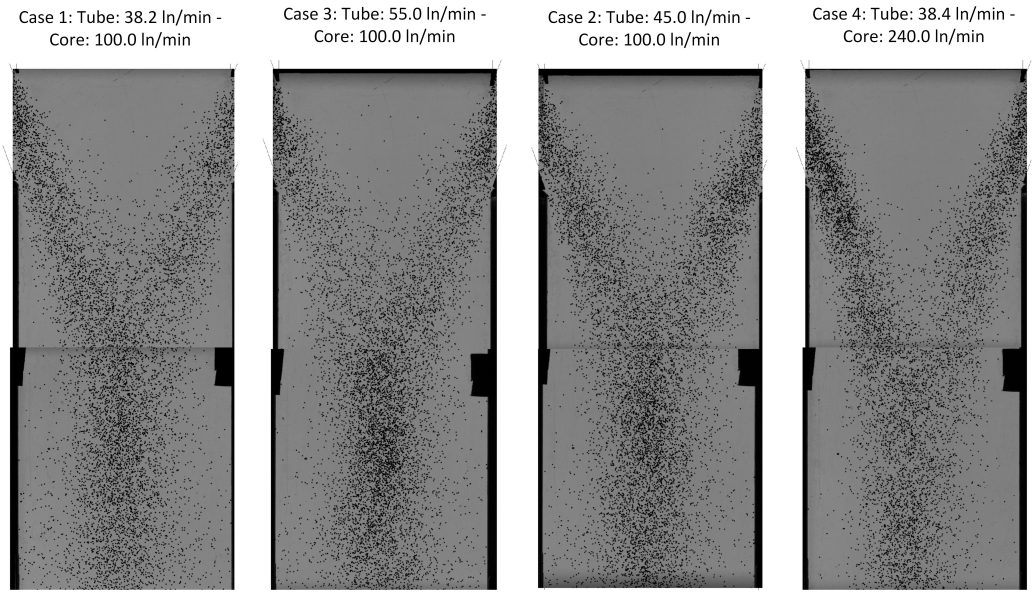

Figure 8: Distribution of the particles over the observation zone recorded for 1st, 2nd, 3th, and 4th case for PSD 300–355 μm

Subsequently, the set of experimental tests were conducted for the fifth and sixth cases (see Tab. 2), with gas flow conditions similar to the fourth case but with larger particles. Figure 9 illustrates the measured velocity profiles in the investigated locations. It can be seen that the lower part of the profile is not fully developed. This is evident when looking at profiles calculated for the second location. Nevertheless, the particle velocity profiles in the third frame were fully developed. The figure 9 results indicate that, because of the large size of the particles,

the time needed to reach the free stream velocity, i.e., ∼26 m/s, is much longer compared to previously discussed cases. Moreover, owing to the wider PSD (see Tab. 1), considerable differentiation can be observed from the calculated standard deviation, indicating that the recurrence of the experiments is less consistent compared to the narrower PSD. This effect is illustrated in Fig. 9 (right).

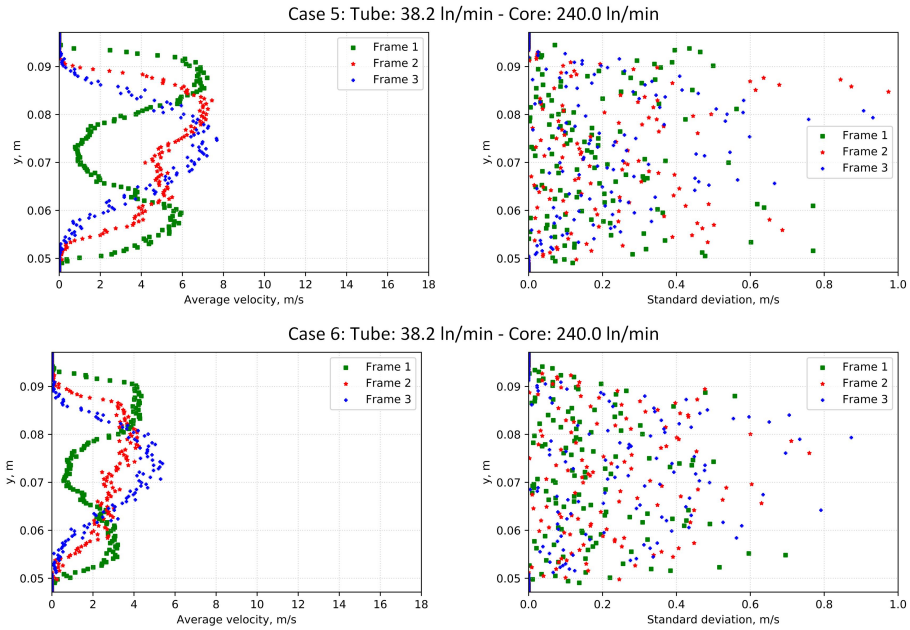

Figure 9: Calculated average particle velocity profiles (left column) and standard deviations (right column) for PSDs 425—500 μm (upper) and 500—600 μm (lower) based on measured velocity profiles during repeatability tests

Figure 10 illustrates particle distribution for each different PSD within the observation region and captured at a time of 0.35 s. The difference between subsequent cases can be noticed in several particles, in the location of the collision region, and the distribution of the particles across the analyzed region. To clarify, the black regions at the top and bottom of the figures indicate the localization of the markers used to combine analyzed image connection. These markers did not influence the flow pattern.

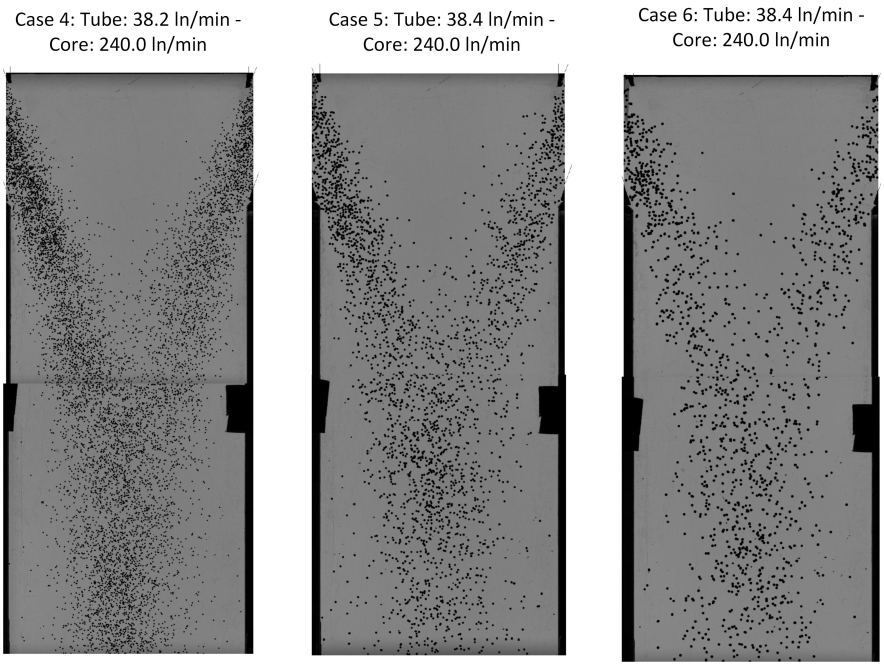

Figure 10: Particle distribution over the measurement region captured at time 0.35s for the investigated cases 4, 5 and 6

4. Numerical model

A set of numerical results was collected to investigate the numerical model, applying DEM approach for the prediction of particle flow patterns in the built test-rig. As mentioned earlier, this work should be seen as a preliminary step towards developing a new particle collision model based on the reduced order model (ROM). The surrogate model will be developed in the framework of the discreet element model, which will be used for generating input data for ROM development. In this stage, the benchmark cases were developed for farther analysis the accuracy of developed collision model based on application of the Deep Machine Learning technique. To developed required cases the numerical results obtained from DEM simulations are compared for both the experimental and numerical results. In future the developed collision model should considerably speed up the simulation for large scale processes. The purpose of the new collision model development is to maintain the time of numerical simulation at the level of the hybrid Euler-Lagrange approach while replacing the kinetic theory of granular flow by the surrogate model with the accuracy of the DEM approach.

4.1. Mathematical model

In the presented work, the accuracy of the DEM approach is investigated and compared with the experimental data. Here, a brief mathematical description of the DEM technique is given, while more detailed information can be found in [42, 11, 43, 44]. The DEM approach is applied by modeling the gas flow with the Eulerian approach, whereas the particles are tracked within the Lagrangian frame of reference [45]. The interactions between the gaseous and particle phase are taken into account using interphase exchange terms together with source terms to control the momentum transfer between the phases. The continuity (6) and momentum (7) equations for the gaseous phase are defined as

$$\frac{\partial}{\partial \tau}\left(\varepsilon_f \rho_f\right) + \nabla \cdot \left(\varepsilon_f \rho_f \mathbf{u}_f\right) = 0 \tag{6}$$

$$\frac{\partial}{\partial \tau}\left(\varepsilon_f \rho_f \mathbf{u}_f\right) + \nabla \cdot \left(\varepsilon_f \rho_f \mathbf{u}_f \mathbf{u}_f\right) = -\varepsilon_f \nabla p + \nabla \cdot \sigma_f + \varepsilon_f \rho_f \mathbf{g} + K_{sf}\left(\mathbf{u}_s - \mathbf{u}_f\right) + S_{\text{mom}} \tag{7}$$

where the subscripts f and s denote the fluid and solid phases, respectively, ρ is the fluid density, $\mathbf{u}$ the velocity vector, and ε_f is the volume fraction of gaseous phase. S_{mom} is the source due to exchange of momentum between the continuous phases and particles, K_{sf} the average interphase drag coefficient, σ_f in Eq. (7) is the stress tensor calculated for gaseous phase and defined as [46] $\sigma_f = \varepsilon_f \mu_f \left(\nabla \mathbf{u}_f + \nabla \mathbf{u}_f^T\right)$, where μ_f represents the fluid dynamic viscosity. In this equation due to the assumption that fluid is treated as incompressible one the terms responsible for modeling bulk phase can be neglected. A detailed description of the DEM approach can be found in [44, 45, 11, 47, 48].

The DEM approach implemented in Ansys Fluent gives possibility to solve the motion equation for a single or a group of particles collected to a single parcel. The equation of particle motion, which equates particle's inertia with forces acting on the particle is defined as

$$\frac{\mathrm{d}\mathbf{u}_p}{\mathrm{d}\tau} = F_{\text{D}}(\mathbf{u}_g - \mathbf{u}_p) + \frac{\mathbf{g}(\rho_p - \rho_g)}{\rho_g} - \frac{\nabla p}{\rho_p} + F_{\text{coll}} + F_{\text{fric}} + F_{\text{add}} \tag{8}$$

where the subscript p denotes the particle, ρ_p the material density, $F_{\text{D}}(\mathbf{u}_f - \mathbf{u}_s)$ the particle acceleration due to gas phase drag force, term $-\nabla p/\rho_f$ defines the particle acceleration due to the pressure difference at the particle location, and F_{coll} the acceleration of the particle due to the collision forces that acts between particles, F_{fric} is the friction force calculated between colliding particles, and F_{add} is the term where all additional forces can be added, i.e. rolling, rotation, lift, thermophoretic, etc. The DEM model is highly sensitive to the mass, diameter, and number of particles in a parcel. The diameter of a parcel is a function of the number of particles that are stored in parcel. All above mentioned parameters are factors in gas-solid drag force acting on the parcels, which in case of simplifications results in overprediction of calculated forces. To reproduce realistic behavior between particles, the parcel should contain only single particle, significantly increasing the need of computational resources able to handle calculations of individual collisions. In case of modeling large-scale devices, where the number of particles reaches billions, usage of detailed DEM approach is practically impossible with current computational techniques. By analyzing group of particle in parcel the simulation accuracy is affects, since it gives only an approximation of the particle behavior during collisions, and in most cases as it was mentioned such situation should be prevented. Based on the calculated particle velocity from equation (8), a new position of the particle can be calculated as

$$\frac{\mathrm{d}\mathbf{x}_p}{\mathrm{d}\tau} = \mathbf{u}_p \tag{9}$$

After obtaining the particle position, the solid volume fraction ε_s in a given numerical cell can be calculated as

$$\varepsilon_s = \frac{\sum_{i=1}^{N_{\text{parcels}}} V_{p,i} n_{\text{p},i}}{V_{\text{cell}}} \tag{10}$$

where V_p is the considered particle volume and V_{cell} the numerical cell volume. The calculated solid volume fraction is assigned to the Eulerian grid, where the bulk phase volume fraction can be determined as $\varepsilon_f = 1 - \varepsilon_s$, and N_{parcels} stands for the number of particle in parcel if applicable. Calculated bulk phase volume fraction is used in momentum equation (7) in order to take into account presence of solid phased within computational domain.

4.2. Collision model

In this work, the Cundall and Stack [49] linear spring-dashpot collision model, a derivation of the soft-sphere technique, was used for accurate prediction of the interaction between particles. The model considers the deformation and shape of the particles resulting from the collision process. In the discussed approach, the collision between particles was controlled by a material spring constant K, N/m. The general idea of the model used for the prediction collision is depicted in Fig. 11.

The collision term in Eq. (8) for DEM assumes

$$F_{\text{coll}} = \vec{F}_1 = -F_2 = (K\delta + \gamma(\mathbf{u}_{p,12}\mathbf{e}_{12}))\mathbf{e}_{12} \tag{11}$$

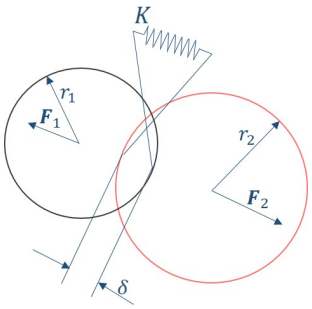

Figure 11: Exaggerated visualization of interparticle collision

where K is the spring constant, γ is the damping coefficient, and δ is the overlap distance (see Fig. 11), defined as $||\mathbf{x}_2 - \mathbf{x}_1|| - (r_1 + r_2)$, $\mathbf{u}_{p,12}$ the relative velocity $(\mathbf{v}_2 - \mathbf{v}_1)$, and $\mathbf{e}_{12}$ represents the unit vector from particle 1 to particle 2, which can be calculated using the simple expression

$$\mathbf{e}_{12} = \frac{\mathbf{x}_2 - \mathbf{x}_1}{||\mathbf{x}_2 - \mathbf{x}_1||} \tag{12}$$

where x_1 and x_2 are the positions of the particle centers. The damping coefficient in Eq. (11) can be calculated as:

$$\gamma = -2\frac{m_{12}\ln\eta}{\tau_{\text{coll}}} \tag{13}$$

where τ_{coll} defines the collision time scale, i.e., $f_{\text{loss}}\sqrt{\frac{m_{12}}{K}}$, and the energy loss factor f_{loss} is expressed using the relation $\sqrt{\pi^2 + \ln^2\eta}$ while η is the coefficient of restitution for the dashpot term, which assumes a value from zero to unity. m_{12} in the above relations is the *reduced mass*, calculated as

$$m_{12} = \frac{m_1 m_2}{m_1 + m_2} \tag{14}$$

Additionally, frictional force between colliding particles is defined as

$$F_{\text{fric}} = \alpha F_{\text{n}} \tag{15}$$

where α denotes the friction coefficient which a function of the relative tangential velocity magnitude [46, 50, 51] and F_{n} is the normal force which is normal to the particle surface or pointing from one particle center to another.

4.3. Numerical model setup

The computational domain is shown in Fig. 12, limited to only a selected part of the injection system and core section. Such simplifications enable a solution to be obtained within a reasonable computational time. Figure 12 illustrates the locations of all inlets, as well as the numerical grid used for the simulation. The computational domain was discretized using hexagonal elements, with a skew factor below 0.22 (average: $4.092{\cdot}10^{-2}$) which, for a given configuration, generates 103 548 elements. The phase-coupled SIMPLE solver [52, 53] was used in the calculations. A second-order discretization scheme was used for the momentum equation. The QUICK scheme [52, 54] was used for the continuity equation and a first-order implicit scheme was used for time discretization. To compare both numerical and experimental results, the time step size for the fluid phase was the same as the time used during the experiment: $\Delta\tau = 7.143 \cdot 10^{-5}$ s. The viscosity of the fluid was taken into account when applying the laminar model. The particle interactions with the front and rear walls were modeled using the same spring constant as that used for the transported material. At the outlet the pressure outlet boundary condition was set with defined zero value for static pressure.

To minimize the complexity of the DEM model, all discussed in the paper simulations were conducted using single particle PSD, mainly the monodisperse particles with a mean size of 315 μm, as shown in Tab. 1. At

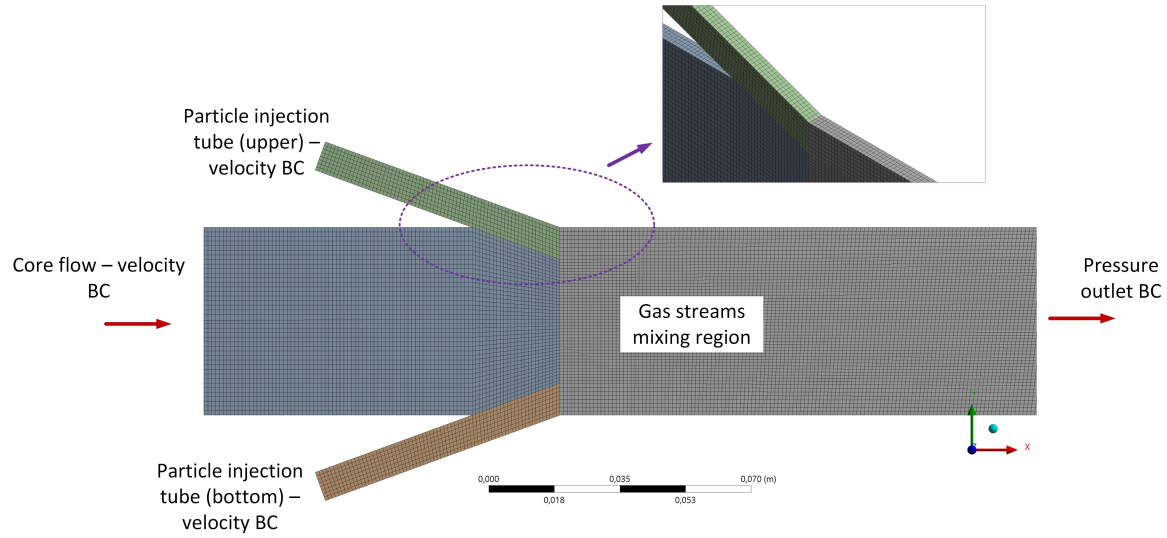

Figure 12: Numerical model with mesh and marked boundary types used for performing simulations and testing the mathematical model

the particle injection tubes (see Fig. 12, the volumetric flow rates of air were set to 38.4 ln/min, while for core section the 100.0 ln/min was defined where three values of spring constant K: 1 000, 6 000, and 10 000 N/m were investigated. Under these conditions, the superficial velocity of the gaseous phase behind the mixing region should reach ∼14.75 m/s. In order to provide required amount of gases into the computational domain the velocity boundary conditions were defined at the inlets, 20 m/s ($A_t = 3.2 \cdot 10^{-5}$ m^2) and 8.35 m/s ($A_c = 2.0 \cdot 10^{-4}$ m^2) for injection tubes and core section, respectively. In simulation constant air density was assumed, equal to 1.22 kg/m^3. An additional simulation was conducted using particles 300—355 μm and the volumetric flow rates were set to 38.4/240.0 ln/min that corresponds to case 4 (see Tab. 2). In that particular case air velocity at the subsequent boundaries was set to 20 m/s. This simulation was carried out to verify the prediction of particle distribution by the DEM for higher gas velocities. The spring constant for the investigated case was set to 6 000 N/m, the friction force was considered.

The particle holders (see Fig. 2) were not included in the numerical model and hence it was necessary to define the exact number of particles carried by the air from the inlet to the injection branches. The number of injected particles through subsequent injection tubes was determined by application a dedicated procedure developed in NI LabVIEW [34], allowing the number of particles injected into the observation zone to be monitored. The average number of injected particles for every time step was 22 and 25, for the upper and bottom streams, respectively, looking at the model configuration while comparing the left and right orientation for test-rig configuration, respectively.

5. Numerical results

The calculated velocity profiles from the numerical simulations were compared with the measured average particle velocity profiles determined applying procedure for tracking particle velocity. Figure 13 illustrates the set of results for Case 1 (38.4/100.0 ln/min). A set of simulations was conducted with three values of spring constant K: 1 000, 6 000, and 10 000 N/m. Based on the obtained numerical results, it can be observed that by decreasing the value of the spring constant K, the elasticity of the particle collisions decreases. The effect can be seen for the smallest investigated value K 1 000, first in the position of the collision region within the domain and second in the distribution of the particles after their collision (accumulation zone, see Fig. 14). This effect is also seen when looking at the profiles downstream from contact streams zones, mainly for the third frame. Calculated profiles is narrowed in contrary to experimental data. This situation changes increasing value of collision model parameters. For spring constants 6 000 and 10 000 N/m the differences are less visible. The

largest discrepancies between the numerical and experimental data can be seen within the first analyzed frame, mainly in the vicinity of the axial symmetry of the domain where analyzed frame passed two particles streams. Figure 13 illustrates that the discrepancies in the first frame decreases with increasing elasticity of the particles approaching experimental data. This means that in order to obtain feasible results the model constant need to be carefully defined. The same effect is seen in Fig. 14 looking only on particle distribution of the material in 0.035 s of the numerical simulation. The discrepancies between the numerical and experimental data on the localization of the collision region are observed in the first frame. With a small value of K, a larger concentration of particles can be seen in the axial vicinity of the computational domain. It is evident that an error made in the definition of the exact value of K, especially for lover values where particle elasticity is reduced can affect the accuracy of the numerical model. For larger values this effect is mitigated for considered cases. In very dense particle flow large values of spring constant will leads to large dispersion of the particle over the computational domain due to the collision.

Analyzing profiles presented in Fig. 13 some asymmetry can be seen in numerical results. Based on observation of the particle movement, due to the collision larger concentration of the particle can be seen at the bottom zone of the domain. In model configuration it was assumed that detection of particle that can colliding was done in size of numerical grid. This for sure affect obtained results and cause some asymmetry in numerical profiles. It is worth to investigate this effect in future work.

The discrepancies between experimental data and numerical can be also caused by providing assumption that only single, mean particles size form PSD will be used in simulations. Including real PSD in DEM can leads to long calculation time also providing some instability in the model. Nevertheless, in farther work it is worth to investigate how PSD can affect calculate particle velocity profile. For sure for larger particle the momentum response time is much longer in contrary to smaller one [11]. In case when particle with large diameter are stored in investigated box (see Fig. 5) used to calculate average particle velocity, calculated value of the velocity is shifted to smaller value while smaller particles this situation will be opposite. In order to check this additional set of simulation should be carried out to investigate sensitivity of the numerical model on defined particle size.

To demonstrate the differences between the first and fourth cases, both are illustrated in Figure 15. For both cases, the profile development process, as well as the acceleration of the particles, can be observed. Analyzing the data, a very good match between the simulation and measurements is achieved for the fourth case. The simulated velocity profiles accurately fit the experimental and manually-calculated data in each location. The manually-calculated velocity is the average velocity of the particles located in subsequent frame calculated based on observation of the particle position form frame to frame. This also gives possibility to check if automatic procedure used for tracking particles was developed properly. The greatest discrepancies between numerical predictions and those measured experimentally can be seen for the first case at the first location. This was caused by the particle spread at the connection of the injection tubes with the core channel. Moving away from this region, the profiles begin to stabilize. For a higher core velocity, the colliding particles are pushed by the core gas back to the injection streams, preventing their dispersal in the vicinity of the connection regions. The asymmetrical effect which is observed for earlier discussed first case is not so visible in case of higher velocity within the core section of the rig which here approach $\sim$5 m/s (almost 10 m/s larger than in first case). High velocity pushed particles downstream into outlet direction mitigating in-perfection of the collision model which can cause asymmetry in case of large number of particles. In order to check how the DEM model deal with situation where small number of particles are colliding, a simple simulation were carried out. In that case evenly distributed particle in two streams were tested. Simulation shown that particle profile, and distribution of particles after collision is symmetrical. Problem arise when asymmetry is observed in colliding streams, which is the case of discussed here configurations. Particles are not evenly redistributed at the inlet to the computational domain prescribed to injection tubes. In model setup only number of particles, their diameter and velocity were defined. Algorithm statistically redistributed particles at the boundary which also affect asymmetry in numerical results.

6. Summary

Nowadays, enormous effort in the engineering community is focused on developing fast, stable, and robust numerical models that can be effectively used for modeling particle transport within various applications. Such models are used to improve the production process, which can lead to a reduction in energy consumption.

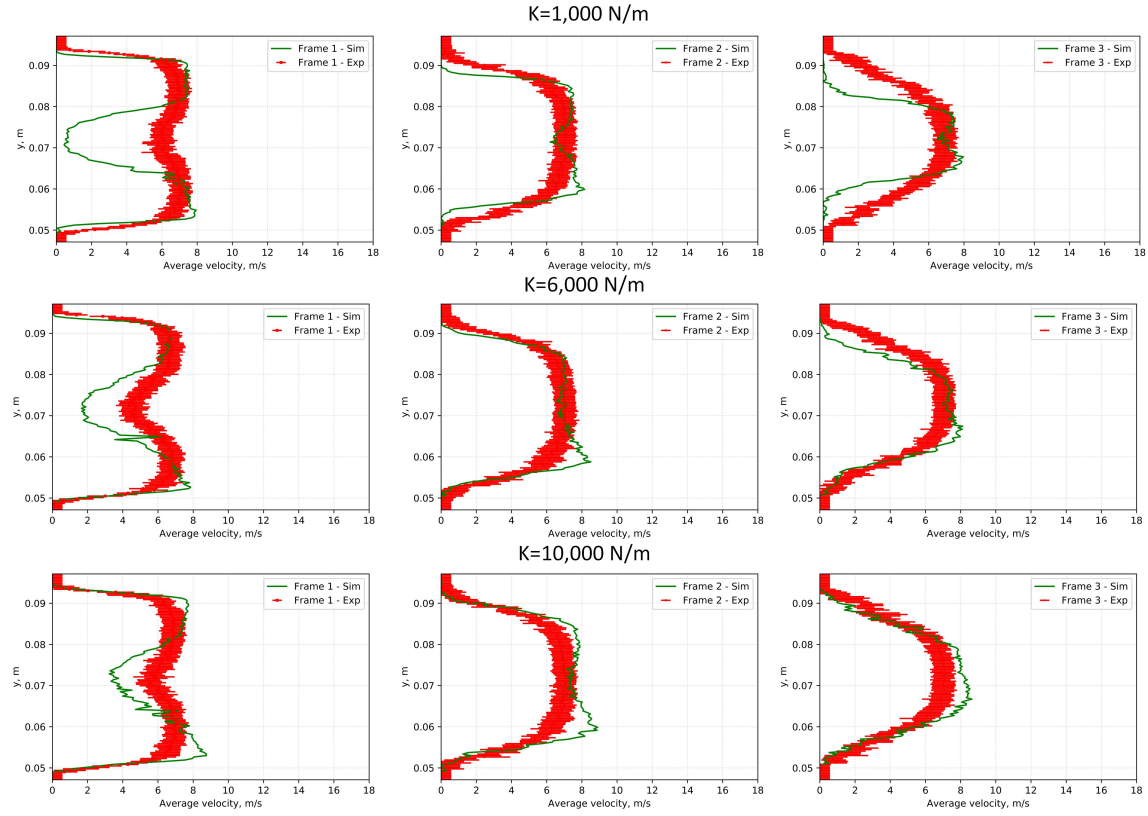

Figure 13: Comparison of the experimental and numerical data (Case 1: 38.4/100.0 ln/min, PSD 300–355 μm) based on the particle velocity profiles calculated for subsequent frames for spring constant: 1,000 (upper), 6,000 (middle), and 10,000 (bottom) with including the friction force

The presented paper provides valuable data collected at novel test-rig configurations that can be applied in terms of testing and validating the developed numerical models. For testing perfectly spherical polyethylene, particles classified into three particle distribution functions were selected. In addition to changing only particle size, the impact of different volumetric flow rates of gases delivered to the rig in the particle transport process was also investigated. For each investigated case, the measurement procedure was repeated three times to ensure the repeatability of the operation, which was a necessary step to determine the uncertainty of the experimental results. Based on the collected data, the average velocity profiles for the particles were determined within three selected locations using an in-house tracking procedure. To determine the error for each analyzed case, the uncertainty calculation was performed, accounting for the influence of various parameters.

The second part of the presented paper focused on numerically modeling the particulate flow by applying the discrete element method (DEM) and investigating the influence of model parameters, i.e. the material spring constant (K), to check its influence on calculated distribution of the particles within the computational domain. Carried out numerical results for three values o spring constant shown the influence how the spring constant affect elasticity of the particles during collision. Evaluated data for two values of mass flow air of air delivered to the rig shown satisfactory accuracy. To check this uncertainty of experimental data also was taken into account while comparing numerical results with experimental.

The collected experimental data, as well as the available numerical results, will be used for testing the new collision model. Numerical model will be farther treated as the benchmark case used to validate developed new collision model. The purpose of farther study is to replace the standard model developed based on the kinetic theory of granular flow (KTGF) for modeling the interaction between particles by a more efficient model, especially when using the hybrid Euler–Lagrange technique. The modified hybrid Euler–Lagrange approach provides

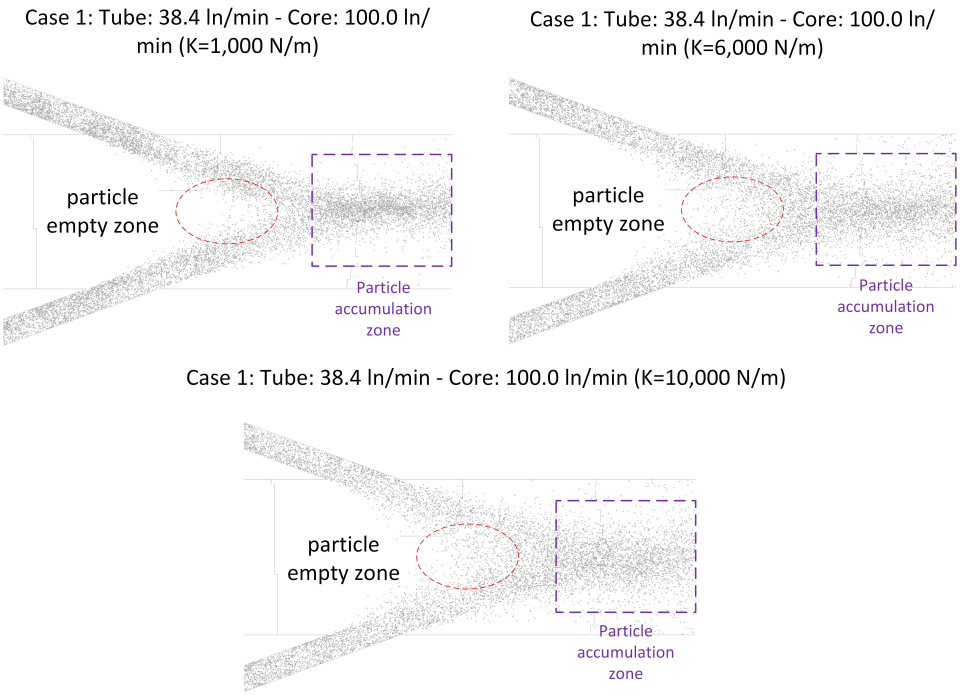

Figure 14: Comparison of the particle flow pattern in 0.035 s of the simulation for investigated values of the spring constant K, where in simulation the friction force was included

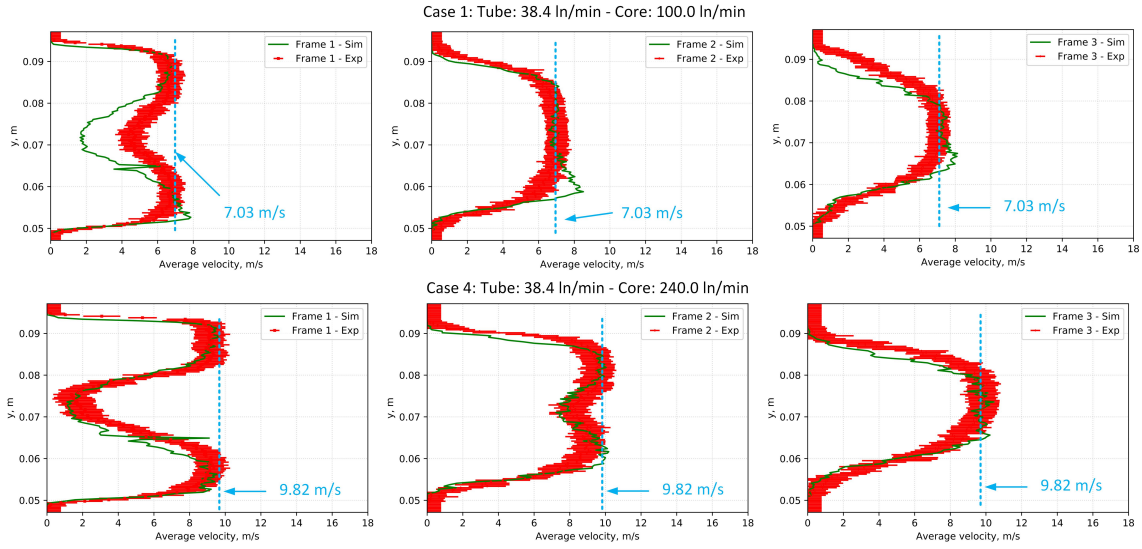

Figure 15: Comparison of the experimental and numerical results based on the particle velocity profiles calculated at three selected locations for 1st and 4th cases

the possibility of effectively simulating large-scale processes with the accuracy of the DEM approach in terms of predicting particle collision. A new model will be developed in the framework of a reduced-order technique by applying a machine learning approach. Moreover, by application of validation and uncertainty quantification procedure the influence of uncertainty in experimental data as well as in assumed mathematical and numerical model parameters on predicted results by the model will be investigated.

Acknowledgments

This research was supported by the National Science Center within the OPUS scheme under contract 2018/31/B/ST8/02201.The authors would also like to acknowledge the financial support for this research from the Academy of Finland, Finland under Grant No. 278641.

References

[1] R. Wischnewski, L. Ratschow, E.-U. Hartge, J. Werther, Reactive gas-solids flows in large volumes 3d modeling of industrial circulating fluidized bed combustors, Particuology 8 (2010) 67–77.
[2] H. E.U., R. L., W. R., W. J., CFD-simulation of a circulating fluidized bed riser, Particuology 7 (2009) 23–296.
[3] M. Farid, H. Jeong, K. Kim, J. Lee, D. Kim, J. Hwang, Numerical investigation of particle transport hydrodynamics and coal combustion in an industrial-scale circulating fluidized bed combustor: Effects of coal feeder positions and coal feeding rates, Fuel 192 (2017) 187–202.
[4] S. Laín, M. Sommerfeld, Numerical calculation of pneumatic conveying in horizontal channels and pipes: Detailed analysis of conveying behaviour, International Journal of Multiphase Flow 39 (2012) 105 – 120. doi:https://doi.org/10.1016/j.ijmultiphaseflow.2011.09.006.
URL http://www.sciencedirect.com/science/article/pii/S0301932211002060
[5] M. Ernst, M. Sommerfeld, S. Laín, Quantification of preferential concentration of colliding particles in a homogeneous isotropic turbulent flow, International Journal of Multiphase Flow 117 (2019) 163 – 181. doi:https://doi.org/10.1016/j.ijmultiphaseflow.2019.05.007.
URL http://www.sciencedirect.com/science/article/pii/S030193221830805X
[6] A. Klimanek, W. Adamczyk, S. Kallio, P. Kozołub, G. Węcel, A. Szlęk, Experimental and numerical study of pseudo-2d circulating fluidized beds, Particuology 29 (2016) 48 – 59. doi:https://doi.org/10.1016/j.partic.2015.09.009.
URL http://www.sciencedirect.com/science/article/pii/S1674200115002035
[7] S. Shah, K. Myöhänen, S. Kallio, T. Hyppänen, CFD simulations of gas-solid flow in an industrial-scale circulating fluidized bed furnace using subgrid-scale drag models, Particuology 18 (2015) 66–75.
[8] W.P. Adamczyk, Application of the Numerical Techniques for Modelling Fluidization Process Within Industrial Scale Boilers, Archives of Computational Methods in Engineering 10 (2016) 1–34.
[9] X. Shi, X. Lan, F. Liu, Y. Zhang, J. Gao, Effect of particle size distribution on hydrodynamics and solids back-mixing in cfb risers using cpfd simulation, Powder Technology 266 (2014) 135 – 143. doi:https://doi.org/10.1016/j.powtec.2014.06.025.
URL http://www.sciencedirect.com/science/article/pii/S0032591014005695
[10] S. Kraft, F. Kirnbauer, H. Hofbauer, Cpfd simulations of an industrial-sized dual fluidized bed steam gasification system of biomass with 8mw fuel input, Applied Energy 190 (2017) 408 – 420. doi:https://doi.org/10.1016/j.apenergy.2016.12.113.
URL http://www.sciencedirect.com/science/article/pii/S0306261916318918
[11] C. Crowe, J. Schwarzkopf, M. Sommerfeld, Y. Tsuji, Multiphase flows with droplets and particles, Taylor & Francis Group, 2012.
[12] J. Lin, K. Luo, S. Wang, C. Hu, J. Fan, An augmented coarse-grained cfd-dem approach for simulation of fluidized beds, Advanced Powder Technology 31 (10) (2020) 4420 – 4427. doi:https://doi.org/10.1016/j.apt.2020.09.014.
URL http://www.sciencedirect.com/science/article/pii/S0921883120304337
[13] D. Gidaspow, Multiphase Flow and Fluidization, Academic Press, Boston, MA., 1994, reaction Engineering International.
[14] S. Cloete, S. Amini, Implementing the kinetic theory of granular flows into the lagrangian dense discrete phase model, 12th International Conference on CFD in Oil Gas, Metallurgical and Process Industries 291 (2017).
[15] S. Chapman, T. Cowling, The mathematical theory of non-uniform gases, 3rd Edition, Cambridge Univ. Press, Cambridge, 1970.
[16] Y. Zhao, B. Lu, Y. Zhong, Influence of collisional parameters for rough particles on simulation of a gas-fluidized bed using a two-fluid model, International Journal of Multiphase Flow 71 (2015) 1–13.
[17] K. Luo, S. Yang, J. Tan, J. Fan, LES-DEM Investigation of Dense Flow in Circulating Fluidized Beds, Procedia Engineering 102 (2015) 1446–1455.
[18] S. Wang, K. Luo, C. Hu, J. Fan, CFD-DEM study of the effect of cyclone arrangements on the gas-solid flow dynamics in the full-loop circulating fluidized bed, Chemical Engineering Science 172 (2017) 199–215.
[19] M. Jebahi, D. Andre, I. Terreros, I. Iordanoff, Numerical Methods in Engineering Series, Wiley, 2015, iSBN: 978-1-848-21770-6.
[20] C. Meyer, D. Deglon, Particle collision modeling – a review, Minerals Engineering 24 (8) (2011) 719–730. doi:https://doi.org/10.1016/j.mineng.2011.03.015.
URL https://www.sciencedirect.com/science/article/pii/S089268751100104X
[21] C. Henry, J.-P. Minier, M. Mohaupt, C. Profeta, J. Pozorski, A. Tanière, A stochastic approach for the simulation of collisions between colloidal particles at large time steps, International Journal of Multiphase Flow 61 (2014) 94 – 107. doi:https://doi.org/10.1016/j.ijmultiphaseflow.2014.01.007.
URL http://www.sciencedirect.com/science/article/pii/S0301932214000135
[22] P. Jacquier, A. Abdedou, V. Delmas, A. Soulaïmani, Non-intrusive reduced-order modeling using uncertainty-aware deep neural networks and proper orthogonal decomposition: Application to flood modeling, Journal of Computational Physics 424 (2021) 109854. doi:https://doi.org/10.1016/j.jcp.2020.109854.
URL https://www.sciencedirect.com/science/article/pii/S0021999120306288
[23] Y. Liu, X. Sun, N. T. Dinh, Validation and uncertainty quantification of multiphase-cfd solvers: A data-driven bayesian framework supported by high-resolution experiments, Nuclear Engineering and Design 354 (2019) 110200, special Issue on TRENDS AND PER-

SPECTIVES IN NUCLEAR THERMAL-HYDRAULICS. doi:https://doi.org/10.1016/j.nucengdes.2019.110200.
URL https://www.sciencedirect.com/science/article/pii/S0029549319302092
[24] D. Mondal, S. Kallio, H. Saxen, J. Hassel, Experimental study of cluster properties in a two-dimensional fluidized bed of geldart b particles, Powder Technology 291 (2015) 420–436.
[25] A. C. Varas, E. Peters, J. Kuipers, Cfd-dem simulations and experimental validation of clustering phenomena and riser hydrodynamics, Chemical Engineering Science 169 (2018) 246 – 258.
[26] R. W. Breault, An analysis of clustering flows in a cfb riser, Powder Technology 220 (2012) 79–87.
[27] C. You, H. Zhao, Y. Cai, H. Qi, X. Xu, Experimental investigation of interparticle collision rate in particulate flow, International Journal of Multiphase Flow 30 (9) (2004) 1121 – 1138. doi:https://doi.org/10.1016/j.ijmultiphaseflow.2004.05.009.
URL http://www.sciencedirect.com/science/article/pii/S0301932204000734
[28] X. Wang, F. Jiang, X. Xu, B. Fan, J. Lei, Y. Xiao, Experiment and CFD simulation of gas solid flow in the riser of dense fluidized bed at high gas velocity, Powder Technology 199 (2010) 203–212.
[29] E. Ghasemi Ardi, K. Dong, A. Yu, R. Yang, A combined experimental and dem approach to determine the breakage of particles in an impact mill, Powder Technology 318 (2017) 543–548. doi:https://doi.org/10.1016/j.powtec.2017.06.026.
URL https://www.sciencedirect.com/science/article/pii/S0032591017304850
[30] B. Quintero, S. Laín, M. Sommerfeld, Derivation and validation of a hard-body particle-wall collision model for non-spherical particles of arbitrary shape, Powder Technology 380 (2021) 526–538. doi:https://doi.org/10.1016/j.powtec.2020.11.032.
URL https://www.sciencedirect.com/science/article/pii/S0032591020310858
[31] M. Sommerfeld, S. Lain, Stochastic modelling for capturing the behaviour of irregular-shaped non-spherical particles in confined turbulent flows, Powder Technology 332 (2018) 253–264. doi:https://doi.org/10.1016/j.powtec.2018.03.026.
URL https://www.sciencedirect.com/science/article/pii/S0032591018302171
[32] D. Kretz, S. Callau-Monje, M. Hitschler, A. Hien, M. Raedle, J. Hesser, Discrete element method (dem) simulation and validation of a screw feeder system, Powder Technology 287 (2016) 131–138. doi:https://doi.org/10.1016/j.powtec.2015.09.038.
URL https://www.sciencedirect.com/science/article/pii/S0032591015300851
[33] P. O'Rourke, D. Snider, An improved collision damping time for MP-PIC calculations of dense particle flows with applications to polydisperse sedimenting beds and colliding particle jets, Chemical Engineering Science 65 (2010) 6014–6028.
[34] NI LabVIEW, National Instruments Corp., http://www.ni.com.
[35] ANSYS® ANSYS, https://www.ansys.com.
[36] P. A., T. G., Computational methods for multiphase flows, Cambridge University Press, 2009.
[37] Bronkhorst high-tech b.v.
URL https://www.bronkhorst.com/int/
[38] Vision research, inc.
URL https://www.phantomhighspeed.com/products/cameras/veo/veo710
[39] Cospheric llc.
URL https://www.cospheric.com
[40] H. Ku, Notes on the use of propagation of error formulas, JOURNAL OF RESEARCH of the National Bureau of Standards - C. Engineering and Instrumentation 70C (4) (1966) 263–273.
[41] G. Yue, R. Cai, J. Lu, H. Zhang, From a cfb reactor to a cfb boiler – the review of rd progress of cfb coal combustion technology in china, Powder Technology 316 (2017) 18–28.
[42] O. T. Sreekanth P., Syamlal M., Computational gas-solids flows and reacting systems: theory, methods and practice, Engineering Science Reference IGI Global, 2012, iSBN 978-1-61520-651-2.
[43] C. Crowe, J. Schwarzkopf, M. Sommerfeld, Y. Tsuji, Multiphase flows with droplets and particles, Taylor & Francis Group, 2012, iSBN: 978-1-439-84050-4.
[44] H. Zhou, G. Flamant, D. Gauthier, J. Lu, Lagrangian approach for simulating the gas-particle flow structure in a circulating fluidized bed riser, International Journal of Multiphase Flow 28 (2002) 1801–1821.
[45] T. Tsuji, K. Yabumoto, T. Tanaka, Spontaneous structures in three-dimensional bubbling gas-fluidized bed by parallel DEM-CFD coupling simulation, Powder Technology 184 (2008) 132–140.
[46] ANSYS, Inc., ANSYS FluentOn-line: http://www.ansys.com (2012).
[47] B. Hoomans, J. Kuipers, W. Briels, W. Swaaij, Discrete particle simulation of bubble and slug formation in a two-dimensional gas-fluidized bed: A hard-sphere approach, Chemical Engineering Science 51 (1996) 99–118.
[48] M. Goldschmidt, R. Beetstra, J. Kuipers, Hydrodynamic modelling of dense gas-fluidized beds: Comparison of the kinetic theory of granular flow with 3D hard-sphere discrete particle simulations, Chemical Engineering Science 57 (2002) 2059–2075.
[49] P. Cundall, O. Strack, A discrete element model for granular assemblies, Géotechnique, 1979.
[50] F. Radjaï, F. Dubois, Discrete-element Modeling of Granular Materials, Wiley-ISTE, 2011, iSBN: 978-1-848-21260-2.
[51] B. Chareyre, The Discrete Element Method for Granular Solids, ISTE Press Ltd - Elsevier Inc, 2019, iSBN: 978-1-785-48066-9.
[52] S. Patankar, Numerical Heat Transfer and Fluid Flow, CRC Press., 1980.
URL https://doi.org/10.1201/9781482234213J
[53] J. H. Ferziger, P. Milovan, Computational Methods for Fluid Dynamics, Springer, 1980.
URL https://doi.org/10.1007/978-3-642-56026-2
[54] H. Versteeg, W. Malalasekera, An introduction to computational fluid dynamic, the finite volume method, 2nd Edition, Pearson Education Limited, 2007.